fluids

MDPI

Article

Finite-Volume Adjoint Field Sensitivity of Drag in Carreau and Oldroyd-B Confined Flow Past Bluff Bodies

Xinyi Li [1], Xiaolong Wang [1], Zhaolin Liu [1] and Sai Peng [1,2,*]

[1] School of Mathematics and Computational Science, Xiangtan University, Xiangtan 411105, China
[2] National Center for Applied Mathematics in Hunan, Xiangtan 411105, China
* Correspondence: pscfd@xtu.edu.cn

Abstract

Drag sensitivities quantify how changes in rheological parameters affect the force on a confined body. Continuous adjoints are implemented with finite volumes for creeping Carreau flow and low-Reynolds-number Oldroyd-B flow past cylinders. The Carreau case has a uniform inlet and moving channel walls, whereas the Oldroyd-B case has a parabolic inlet and stationary walls. At Cu = 100 and Wi = 0.5, respectively, the volume-integrated transition-time and relaxation-time sensitivities are compared with independently converged central finite differences. The maximum discrepancies over the tested perturbation sizes are 0.221% for Carreau and 0.418% for Oldroyd-B. Separate three-grid calculations give medium-to-fine drag changes of 0.495% and 0.488%. The Carreau sensitivities are concentrated near the cylinder sides: increasing the transition time reduces drag, while increasing the shear index increases it. The Oldroyd-B relaxation-time response contains positive and negative contributions whose cancellation leaves a small negative integral. Archived sphere calculations provide an additional direct-flow example. The quantitative derivative checks apply to the two cylinder states and do not establish pointwise or three-dimensional sensitivity accuracy.

Keywords: OpenFOAM; Carreau fluid; Oldroyd-B fluid; drag sensitivity; continuous adjoint method; field sensitivity; non-Newtonian flow

1. Introduction

Rheological parameters affect the drag on a confined body through both the constitutive response and the resulting flow field. In a Carreau fluid, the apparent viscosity changes with the local strain rate. In an Oldroyd-B fluid, polymer stress also depends on deformation and transport along the flow [1–3]. Cylinder and sphere configurations provide useful tests of these effects because strong velocity gradients occur near the body while the surrounding flow determines the integrated force. Studies of generalized Newtonian cylinder flow have examined how shear dependence changes drag and wake development [4–7]; viscoelastic benchmarks have also exposed the sensitivity of force predictions to stress transport and numerical stabilization [8–10].

A uniform parameter perturbation gives a global derivative but does not identify the spatial contributions to that derivative. An adjoint calculation provides a field sensitivity for a chosen objective, from which the effect of a small, spatially varying parameter change can be obtained by integration [11–13]. Freund, Kim and Ewoldt [14] applied this approach to rheological parameters for a sphere moving in a tube, including a Carreau fluid. Kim [15] subsequently considered Oldroyd-B flow around a confined cylinder at low Deborah

Check for updates

Academic Editor: Giuliano De Stefano

Received: 30 June 2026
Revised: 28 September 2026
Accepted: 29 September 2026
Published: 10 October 2026

Copyright: © 2026 by the authors. Licensee MDPI, Basel, Switzerland. This article is an open access article distributed under the terms and conditions of the Creative Commons Attribution (CC BY) license.

number. These studies motivate interpreting rheological effects through the combination of constitutive derivatives and drag-adjoint fields.

For a finite-volume implementation, agreement in the direct force does not by itself establish the accuracy of an adjoint derivative. The direct and continuous-adjoint equations are discretized separately, and their operators need not form an exact transpose pair [16]. Spatial refinement and a direct parameter perturbation therefore answer different questions: the first measures changes in drag with resolution, while the second checks an integrated sensitivity against an independently computed force difference. OpenFOAM provides the mesh, field and force-evaluation operations needed for these comparisons [17,18]; established viscoelastic implementations also provide useful numerical context [19,20].

This study presents a finite-volume reproduction of Carreau and Oldroyd-B drag sensitivities with these two checks. Each cylinder configuration is specified independently, including its wall motion, inlet profile and rheological parameters. Three-grid force results and several perturbation sizes accompany the local maps and integrated sensitivities. The Carreau response is interpreted through the viscosity derivatives, and the Oldroyd-B response through the cancellation of signed contributions. Archived confined-sphere calculations are retained for direct-flow context; quantitative sensitivity verification is restricted to the cylinder cases.

Section 2 defines the force and sensitivity expressions. Section 3 gives the numerical configurations and verification procedures. Section 4 presents the force, derivative and field results, followed by their interpretation and limitations in Section 5 and conclusions in Section 6.

2. Governing Models and Drag Sensitivity

2.1. Drag Functional

Let Ω denote the fluid domain and Γ_b the surface of the immersed bluff body. The total surface-integrated drag on the computational body, including the finite extrusion used for a planar case, is written as

$$\mathcal{D} = \int_{\Gamma_b} \boldsymbol{e}_x \cdot \boldsymbol{\sigma} \cdot \boldsymbol{n} \, \mathrm{d}S, \tag{1}$$

where $\boldsymbol{\sigma} = -p\boldsymbol{I} + \boldsymbol{\tau}$ is the physical Cauchy stress, $\boldsymbol{\tau}$ is the total extra stress and $\boldsymbol{e}_x$ is the streamwise unit vector, $\boldsymbol{n}$ is the outward unit normal pointing into the fluid. For a planar extrusion of span L_z, the force per unit span is $\mathcal{D}/L_z$. The same division is applied to an integrated derivative. The verification below uses the total force consistently; a normalized cylinder resistance is $\mathcal{D}/(\eta_{\mathrm{ref}} U L_z)$, with $\eta_{\mathrm{ref}} = \eta_0$ for Carreau and $\eta_s + \eta_p$ for Oldroyd-B.

For a perturbation to one spatially varying rheological parameter $\theta_i(\boldsymbol{x})$, the first variation in drag can be written in the form

$$\delta\mathcal{D} = \int_{\Omega} G_{\theta_i}(\boldsymbol{x}) \, \delta\theta_i(\boldsymbol{x}) \, \mathrm{d}\Omega, \tag{2}$$

where G_{θ_i} is the sensitivity per unit volume, with units $[\mathcal{D}]/([\theta_i]\,\mathrm{m}^3)$. The direct variation of the flow state is eliminated through the adjoint equations. Thus, once the direct and adjoint fields are known, G_{θ_i} gives the local contribution of a unit parameter perturbation to the drag objective.

The continuous-adjoint reduction can be summarized through a Lagrangian,

$$\mathcal{L} = \mathcal{D} + \int_{\Omega} \boldsymbol{u}^{\dagger} \cdot \mathcal{R}_m(\boldsymbol{q}, \boldsymbol{\theta}) \, \mathrm{d}\Omega + \int_{\Omega} p^{\dagger} \mathcal{R}_c(\boldsymbol{q}) \, \mathrm{d}\Omega + \int_{\Omega} \boldsymbol{\chi}^{\dagger} : \mathcal{R}_r(\boldsymbol{q}, \boldsymbol{\theta}) \, \mathrm{d}\Omega, \tag{3}$$

where $\boldsymbol{q}$ denotes the direct flow variables, $\boldsymbol{\theta}$ denotes the rheological parameters, $\mathcal{R}_m$ and $\mathcal{R}_c$ are the momentum and continuity residuals and $\mathcal{R}_r$ is the rheological residual. For a

generalized Newtonian fluid, $\mathcal{R}_r$ is absent because the viscosity is an algebraic function of the strain rate. For the Oldroyd-B fluid, $\mathcal{R}_r$ is the polymer-stress transport equation. The adjoint variables $\boldsymbol{u}^\dagger$, $p^\dagger$ and $\boldsymbol{\chi}^\dagger$ are chosen so that the coefficients of the direct-flow variations vanish. The remaining variation then has the form of Equation (2).

Each parameter sensitivity is stored at cell centers. Summing $G_{\theta_i,K}V_K$ gives the global derivative for a uniform perturbation.

2.2. Carreau Generalized Newtonian Fluid

The strain-rate tensor is $\boldsymbol{D}(\boldsymbol{u}) = [\boldsymbol{\nabla u} + (\boldsymbol{\nabla u})^T]/2$, with $(\boldsymbol{\nabla u})_{ij} = \partial u_i/\partial x_j$. The Carreau viscosity is

$$\eta(\dot\gamma) = \eta_\infty + (\eta_0 - \eta_\infty)\left[1 + (\lambda\dot\gamma)^2\right]^{(n-1)/2}, \tag{4}$$

where η_0 and η_∞ are the zero- and infinite-shear viscosities, λ is a shear-rate transition time scale, n is the shear-index parameter and $\dot\gamma = (2\boldsymbol{D}:\boldsymbol{D})^{1/2}$ is the strain-rate magnitude. The viscous stress is $\boldsymbol{\tau} = 2\eta\boldsymbol{D}$. The Carreau computations use the incompressible creeping-flow equations $\boldsymbol{\nabla}\cdot\boldsymbol{u} = 0$ and $-\boldsymbol{\nabla}p + \boldsymbol{\nabla}\cdot(2\eta\boldsymbol{D}) = 0$; inertia is omitted. The time scale λ in this generalized Newtonian law does not introduce elastic memory.

At fixed strain rate, define

$$A = \left[1 + (\lambda\dot\gamma)^2\right]^{(n-1)/2}. \tag{5}$$

The parameter derivatives are

$$\frac{\partial\eta}{\partial\eta_0} = A, \qquad \frac{\partial\eta}{\partial\eta_\infty} = 1 - A, \tag{6}$$

$$\frac{\partial\eta}{\partial\lambda} = (\eta_0 - \eta_\infty)(n-1)\lambda\dot\gamma^2\left[1 + (\lambda\dot\gamma)^2\right]^{(n-3)/2}, \qquad \frac{\partial\eta}{\partial n} = \frac{1}{2}(\eta_0 - \eta_\infty)A\ln\left[1 + (\lambda\dot\gamma)^2\right]. \tag{7}$$

The dependence on the flow state must also be linearized. At fixed material parameters, the stress variation is

$$\delta\boldsymbol{\tau} = 2\eta\,\delta\boldsymbol{D} + 4b(\boldsymbol{D}:\delta\boldsymbol{D})\boldsymbol{D}, \qquad b = (\eta_0 - \eta_\infty)(n-1)\lambda^2[1 + (\lambda\dot\gamma)^2]^{(n-3)/2}. \tag{8}$$

Here, $b = \dot\gamma^{-1}\partial\eta/\partial\dot\gamma$, with its continuous limit at zero strain rate. This tangent stress is used in the Carreau adjoint operator; freezing the direct state does not mean omitting the strain-rate derivative of viscosity.

With the adjoint convention in Section 3.2, the Carreau sensitivity is

$$G^C_{\theta_i} = Q_\eta(\boldsymbol{x})\,\frac{\partial\eta}{\partial\theta_i}, \qquad \theta_i \in \{\eta_0, \eta_\infty, \lambda, n\}, \tag{9}$$

where $Q_\eta = -2\boldsymbol{D}(\boldsymbol{u}) : \boldsymbol{D}(\boldsymbol{w})/U$ and $\boldsymbol{w}$ is the velocity-scaled adjoint. The same strain kernel gives all four parameter sensitivities. At fixed nonzero strain rate, increasing λ lowers viscosity when $n < 1$, whereas increasing n raises it. The spatial drag response also depends on Q_η, so the constitutive derivative alone does not identify the dominant region.

2.3. Oldroyd-B Viscoelastic Fluid

For Oldroyd-B flow, $\boldsymbol{\tau} = 2\eta_s \boldsymbol{D} + \boldsymbol{\tau}_p$, where $\boldsymbol{\tau}_p$ is the polymer stress. The steady incompressible equations are

$$\boldsymbol{\nabla} \cdot \boldsymbol{u} = 0, \tag{10}$$

$$\rho \boldsymbol{u} \cdot \boldsymbol{\nabla} \boldsymbol{u} = -\boldsymbol{\nabla} p + \boldsymbol{\nabla} \cdot (2\eta_s \boldsymbol{D} + \boldsymbol{\tau}_p), \tag{11}$$

$$\boldsymbol{\tau}_p + \lambda \mathcal{C}(\boldsymbol{\tau}_p) = 2\eta_p \boldsymbol{D}, \tag{12}$$

$$\mathcal{C}(\boldsymbol{\tau}_p) = \boldsymbol{u} \cdot \boldsymbol{\nabla} \boldsymbol{\tau}_p - (\boldsymbol{\nabla} \boldsymbol{u}) \boldsymbol{\tau}_p - \boldsymbol{\tau}_p (\boldsymbol{\nabla} \boldsymbol{u})^T. \tag{13}$$

The operator $\mathcal{C}$ is the steady upper-convected derivative. The parameters η_s, η_p and λ are the solvent viscosity, polymer viscosity and relaxation time, respectively. The Weissenberg number is $\mathrm{Wi} = \lambda U/a$, where a is the cylinder radius and U is the reference mean inlet velocity.

The velocity and polymer-stress adjoints are coupled. With the scaled symmetric stress adjoint $\boldsymbol{z}$ used in the supplied implementation, the cellwise kernels are

$$G_{\eta_s} = \frac{2}{U} \boldsymbol{D}(\boldsymbol{u}) : \boldsymbol{D}(\boldsymbol{w}), \tag{14}$$

$$G_{\eta_p} = -\frac{2}{\eta_p U} \boldsymbol{z} : \boldsymbol{D}(\boldsymbol{u}), \tag{15}$$

$$G_{\lambda} = \frac{1}{\eta_p U} \boldsymbol{z} : \mathcal{C}(\boldsymbol{\tau}_p). \tag{16}$$

The signs and scaling are tied to the boundary conditions stated in Section 3.2. In particular, the velocity adjoint has a different boundary convention from the Carreau case; its sign cannot be transferred between the two kernel definitions. For simultaneous material perturbations,

$$\delta \mathcal{D} = \int_{\Omega} (G_{\eta_s} \delta \eta_s + G_{\eta_p} \delta \eta_p + G_{\lambda} \delta \lambda) \, \mathrm{d}\Omega. \tag{17}$$

Unlike the Carreau transition time, the Oldroyd-B relaxation time acts through polymer-stress transport. The resulting sensitivity need not have one sign throughout the domain. The present implementation is tested at $\mathrm{Wi} = 0.5$; stabilization requirements at higher elasticity are discussed in Section 5.

3. Numerical Configuration

3.1. Numerical Implementation

The cylinder direct, adjoint and perturbation calculations use OpenFOAM Foundation 9. The Carreau solver includes the tangent stress in Equation (8); the Oldroyd-B direct solver combines a Maxwell polymer contribution with a Newtonian solvent. The polymer-stress adjoint is solved with the converged direct velocity and stress held fixed. The case files and solver sources specify the force evaluation, boundary conventions and stopping criteria. Archived foam-extend/rheoTool calculations are identified separately in Section 4.

3.2. Cylinder Geometries and Boundary Conditions

The dimensional case values use SI units: length in m, velocity in $\mathrm{m\,s^{-1}}$, viscosity in Pa s, density in $\mathrm{kg\,m^{-3}}$ and time in s. The Carreau cylinder has radius $a = 1$ in a channel with $-100 \le x/a \le 100$ and $-2 \le y/a \le 2$. The inlet and channel walls move at $U\boldsymbol{e}_x$, with $U = 1$, while the cylinder is fixed. The original outlet is an inlet–outlet velocity condition with the prescribed velocity used for reverse flow; the new O-grid family uses its outflow, zero-gradient branch. Pressure is fixed to zero at the outlet and has zero normal gradient on the other velocity boundaries. The parameters are $\eta_0 = 1$, $\eta_\infty = 0.001$, $n = 0.2$ and $\lambda = 100$, giving $\mathrm{Cu} = \lambda U/a = 100$.

The Oldroyd-B cylinder has $a = 10^{-3}$, $-20 \leq x/a \leq 20$ and the same height ratio $H/a = 4$. The inlet profile is $u_x(y) = 1.5U[1 - (y/(2a))^2]$, with mean reference velocity $U = 1$. The channel walls and cylinder are stationary. The outlet has zero-gradient velocity and zero reference pressure. Polymer stress is prescribed to zero at the inlet and extrapolated on the other boundaries. The parameters are $\eta_s = 0.59$, $\eta_p = 0.41$, $\lambda = 5 \times 10^{-4}$ and $\rho = 1$, giving Wi $= 0.5$ and $\rho Ua/(\eta_s + \eta_p) = 0.001$. Momentum convection is retained in this case. Thus, the comparison between the models is not a controlled change in constitutive law at identical boundary conditions.

The planar verification meshes each contain 17,600 cells and one cell across an empty spanwise direction. Their spans are $L_z = 4.00079992$ and $8.039900496 \times 10^{-4}$ for Carreau and Oldroyd-B, respectively. The meshes are shown in Figures 1 and 2.

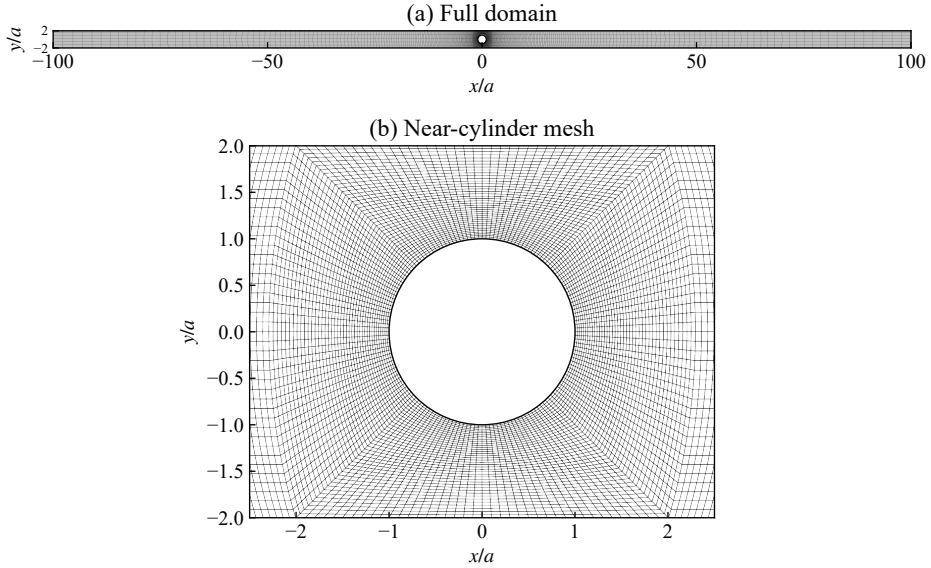


Figure 1. Actual 17,600-cell Carreau verification mesh: full domain and cylinder detail. Both panels use equal horizontal and vertical coordinate scales. Coordinates are divided by the cylinder radius.

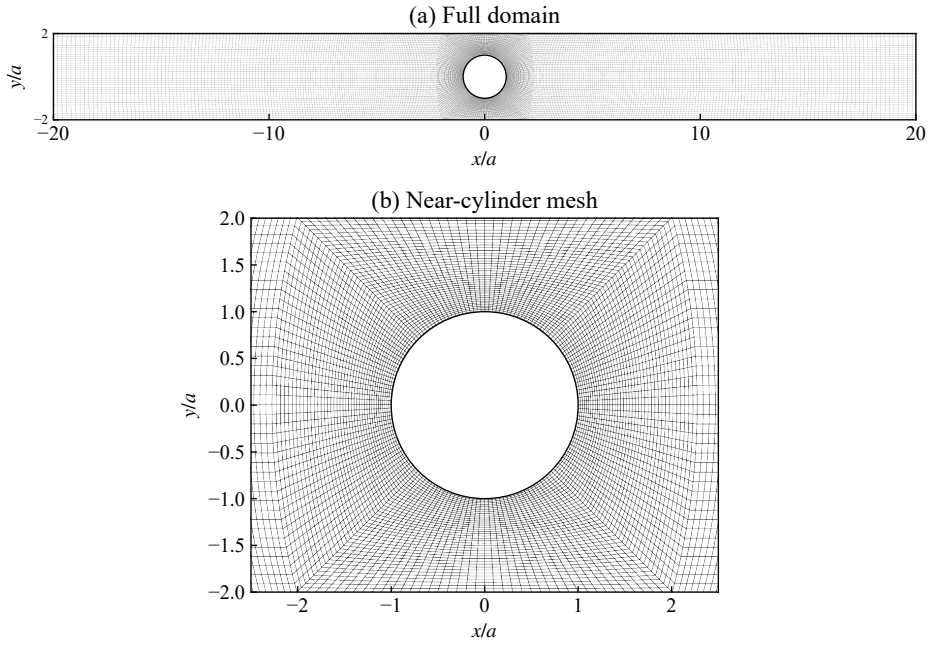


Figure 2. Actual 17,600-cell Oldroyd-B verification mesh: full domain and cylinder detail. Both panels use equal horizontal and vertical coordinate scales. Coordinates are divided by the cylinder radius.

The adjoint velocity convention is $\boldsymbol{w} = 0$ on the Carreau body and $\boldsymbol{w} = -U\boldsymbol{e}_x$ on the outer truncation boundaries. For Oldroyd-B, the adjoint velocity is $-U\boldsymbol{e}_x$ on the body and zero on the outer boundaries; the stress-adjoint transport direction is reversed, with homogeneous data at its inflow (the direct-flow outlet). Adjoint pressure uses a reference cell. These conventions are recorded explicitly in the supplied cases. The finite-difference test measures the error of the implemented integral, including spatial discretization and outer-boundary truncation, rather than assuming an exact discrete-adjoint identity.

3.3. Archived Sphere Configuration

The confined Carreau sphere has radius $a = 2.0 \times 10^{-5}$ in a tube of radius $R = 2a$, with $-50 \leq x/a \leq 50$ and 53,200 cells. The sphere is fixed; the inlet and tube wall move at $U\boldsymbol{e}_x$, with $U = 1$. The illustrated state has $\eta_0 = 1$, $\eta_\infty = 0.001$, $n = 0.2$ and Cu $= 1$. Figure 3 shows the geometry. Only direct fields and forces are used from this archive.

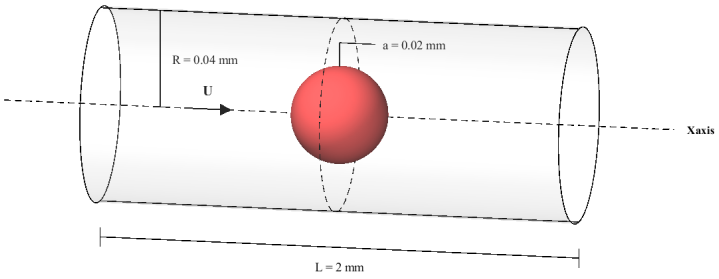


Figure 3. Confined-sphere geometry. The sphere is coaxial with the tube; inlet and tube-wall velocities are the same in the body-fixed frame.

3.4. Output and Normalization

The field plots use normalized spatial coordinates and separate colorbars. Cell-to-vertex interpolation is used for display, whereas integrals use cell-centered values and polyhedral cell volumes. For a planar extrusion, define

$$\widehat{G}_{\theta_i} = \frac{\theta_{i,0} a^2 L_z}{\mathcal{D}_0} G_{\theta_i}, \qquad s_i = \frac{\theta_{i,0}}{\mathcal{D}_0} \sum_K G_{\theta_i,K} V_K. \tag{18}$$

Thus $s_i = \int \widehat{G}_{\theta_i} \, \mathrm{d}(x/a) \, \mathrm{d}(y/a)$ for a spanwise-uniform field. In three dimensions, the analogous factor is a^3. Reference values remain fixed at the unperturbed state. Pressure maps show $pa/(\eta_{\mathrm{ref}} U)$; the OpenFOAM kinematic pressure is converted using the case density.

3.5. Principal Numerical Settings and Convergence

Table 1 lists the cylinder calculation settings. The archived foam-extend/rheoTool dictionaries are identified separately in Supplementary Material S1. The Oldroyd-B polymer variable in the native direct solver, denoted here by $\boldsymbol{\sigma}_{\mathrm{OF}} = -\boldsymbol{\tau}_p/\rho$, differs from the physical Cauchy stress. It is converted back to physical polymer stress before the adjoint solve.

The Carreau solver additionally requires a relative change below 10^{-9} in its surface-traction monitor for 30 consecutive iterations, after at least 100 iterations. The Oldroyd-B adjoint applies the same 30-iteration change criterion to the integrated λ sensitivity. The native Oldroyd-B direct solver stops only when all specified residual controls are met. Reaching the maximum iteration count is not counted as convergence. Convergence histories and the last written fields are included with the cases so that achieved values can be distinguished from prescribed thresholds.

The upwind Oldroyd-B choice follows an observed failure of the less dissipative trial to reach a stationary residual level. That trial is not used in the reported tables. Upwind

transport changes spatial error and therefore requires the accompanying grid study; it is not claimed to be second-order. No artificial polymer-stress diffusion is added in the accepted new runs. The O-grid solutions were continued with the final coupling and relaxation settings listed in the table, consistently at all three levels; their earlier initialization histories are retained with the cases.

Table 1. Principal settings of the cylinder calculations. Absolute/relative tolerances in the linear solves are distinct from the outer residual stopping criterion.

Setting	Carreau	Oldroyd-B
Gradient	Least squares	Gauss linear
Momentum convection	Omitted (creeping flow)	Upwind; reversed transport in adjoint
Polymer/stress-adjoint convection	Not applicable	Upwind
Laplacian/face interpolation	Gauss linear corrected/linear	Same
Time derivative	Steady state	Steady state
Pressure solver	GAMG, Gauss–Seidel smoother	Same
Velocity/stress solver	Symmetric Gauss–Seidel smoothing	PBiCGStab with DILU
Linear absolute/relative tolerance	$10^{-12}/0.01$	$10^{-12}/0.01$
Outer residual threshold	10^{-9} for velocity and pressure	10^{-9} for velocity, pressure and stress
Pressure–velocity coupling	SIMPLE (verification); SIMPLEC (O-grid)	SIMPLE (verification); SIMPLEC (O-grid)
Non-orthogonal corrections	One	One
Pressure relaxation	0.3 (verification); 1 (O-grid)	0.2 (verification); 0.7 (O-grid)
Velocity relaxation	0.7 (direct), 0.5 (adjoint); 0.95 (O-grid)	0.3 (verification); 0.6 (O-grid)
Polymer/stress-adjoint relaxation	Not applicable	0.2 (verification); 0.4 (O-grid)
Field/scalar-history precision	14/15 significant digits	14/full force-history precision

3.6. Mesh and Independent Derivative Verification

The new cylinder grid families contain 4608, 18,432 and 73,728 cells. Each uses eight circular-body blocks and four channel-extension blocks. The angular, radial and extension counts double at every level; the single empty spanwise cell is unchanged. The radial and streamwise grading ratios are held fixed. Arc edges follow the circular body, and all three levels pass the OpenFOAM mesh-quality check. Geometry, material parameters, velocity data and extrusion span are held fixed within each family. The parabolic inlet is evaluated at the inlet-face centers on each Oldroyd-B grid. Its face-area quadrature gives mean velocities $1.00048828U$, $1.00012207U$ and $1.00003052U$, respectively; this decreasing inlet-discretization contribution is included in the reported force convergence. Figure 4 shows the actual near-body refinement.

For a planar systematic refinement the spacing ratio is $r = 2$ and $h \propto N^{-1/2}$. For a monotonic sequence with decreasing increments, the observed order is computed from

$$p_{\mathrm{obs}} = \frac{\ln\left|(\mathcal{D}_c - \mathcal{D}_m)/(\mathcal{D}_m - \mathcal{D}_f)\right|}{\ln 2}. \tag{19}$$

The fine-grid grid convergence index (GCI), expressed as a fraction, is estimated as [21]

$$\mathrm{GCI}_f = \frac{1.25\,|\mathcal{D}_f - \mathcal{D}_m|}{|\mathcal{D}_f|(2^{p_{\mathrm{obs}}} - 1)}. \tag{20}$$

The safety factor is 1.25; the tables and text report $100\,\mathrm{GCI}_f$ as a percentage. This estimate assumes a leading power-law error over the three grids. A monotonic force sequence permits the calculation but does not by itself establish that the asymptotic regime has been reached.

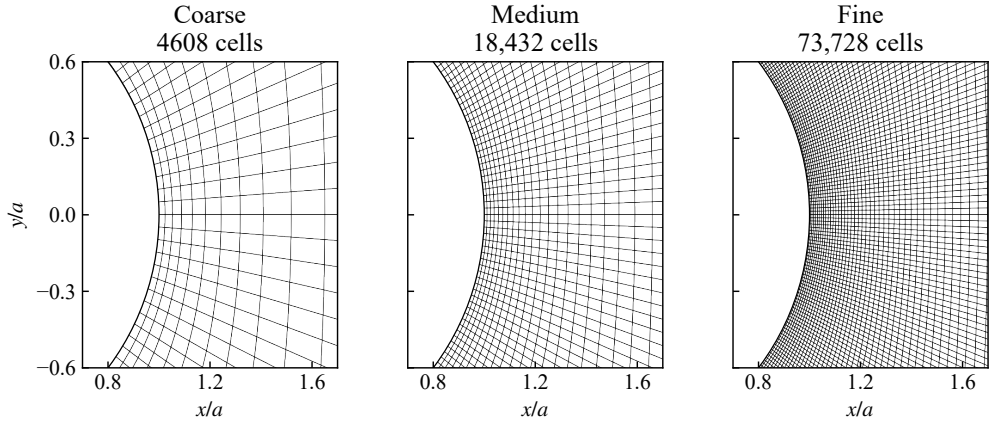


Figure 4. Near-cylinder detail of the new coarse, medium and fine O-grid family. The same dimensionless near-body block construction is used for both fluids; their channel extensions and physical scales differ as specified in Section 3.2. The plotted cells are read from the generated meshes.

The integrated adjoint derivative is checked independently on the original 17,600-cell mesh for each model. For a uniform parameter perturbation,

$$S_i^{\mathrm{AD}} = \sum_K G_{\theta_i,K} V_K, \tag{21}$$

$$S_i^{\mathrm{FD}}(h) = \frac{\mathcal{D}(\theta_{i,0} + h) - \mathcal{D}(\theta_{i,0} - h)}{2h}, \tag{22}$$

$$E_i(h) = \frac{|S_i^{\mathrm{AD}} - S_i^{\mathrm{FD}}(h)|}{|S_i^{\mathrm{FD}}(h)|}. \tag{23}$$

The sum uses each actual polyhedral cell volume. Density, geometry, boundary conditions and every unperturbed parameter are identical within a pair. Both direct solutions are independently converged; a baseline field is used only as an initial guess. The tested relative λ steps are 1%, 0.5% and 0.25% for Carreau, and 1% and 0.5% for Oldroyd-B. Normalization always uses the unperturbed force and parameter, so the test does not inadvertently differentiate a changing reference scale.

The grid study and derivative checks use different mesh families. Their results are compared in Section 4.1.

4. Results

4.1. Mesh Convergence and Independent Integrated Verification

Table 2 gives medium-to-fine drag changes of 0.495% for Carreau and 0.488% for Oldroyd-B. The observed orders are 1.703 and 2.336, respectively. Assuming the leading-error model in Section 3.6, Equation (20) gives fine-grid GCI estimates of 0.274% and 0.151%. The measured order describes this three-grid force sequence, not the formal order of the stress-transport scheme; combined error contributions can give an apparent order

above that of upwind transport. Further refinement would be needed to test whether that behavior persists.

Table 2. Three-grid drag comparison for the two cylinder configurations. The span L_z is fixed within each model. Change is $100|\mathcal{D}_j - \mathcal{D}_{j-1}|/|\mathcal{D}_j|$, where j is the current, finer level. Every reported run meets the residual criterion in Section 3.5.

Model	Mesh	Cells	$\mathcal{D}$ (N)	$\mathcal{D}/L_z$ (N/m)	Change (%)
Carreau	Coarse	4608	4.0104782	1.002419	–
Carreau	Medium	18,432	4.07653906	1.018931	1.6205
Carreau	Fine	73,728	4.09683007	1.024003	0.4953
Oldroyd-B	Coarse	4608	0.0926387961	115.2238	–
Oldroyd-B	Medium	18,432	0.0949904989	118.1488	2.4757
Oldroyd-B	Fine	73,728	0.0954563991	118.7283	0.4881

Tables 3 and 4 give maximum adjoint–finite-difference discrepancies of 0.221% and 0.418% over the tested steps. The finite-difference estimates vary only slightly as the perturbation size decreases. The comparison checks the integrated derivative; it does not resolve local errors that may cancel under volume integration.

Table 3. Integrated derivative check for Carreau on the 17,600-cell cylinder mesh. The volume-integrated adjoint value is $S_\lambda^{\mathrm{AD}} = -0.02874258$ N/s. Forces are in N and derivatives are in N/s; E is defined in Equation (23).

h/λ_0	$\mathcal{D}(\lambda_0 - h)$	$\mathcal{D}(\lambda_0 + h)$	S_λ^{FD}	$100E$ (%)
0.01	4.1247564974	4.0671442545	−0.028806121	0.2206
0.005	4.1101593501	4.0813557562	−0.028803594	0.2118
0.0025	4.1029097777	4.0885089267	−0.028801702	0.2053

Table 4. Integrated derivative check for Oldroyd-B on the 17,600-cell cylinder mesh. The volume-integrated adjoint value is $S_\lambda^{\mathrm{AD}} = -4.6286105$ N/s. Forces are in N and derivatives are in N/s; E is defined in Equation (23).

h/λ_0	$\mathcal{D}(\lambda_0 - h)$	$\mathcal{D}(\lambda_0 + h)$	S_λ^{FD}	$100E$ (%)
0.01	0.096336983405	0.096290503101	−4.6480304	0.4178
0.005	0.096324581073	0.096301351962	−4.6458221	0.3705

The 17,600-cell verification meshes are not members of the new O-grid sequences. Their baseline forces are 4.0956932854 and 0.096312707213. Relative to the corresponding finest O-grid forces, the differences are 0.028% and 0.897%, respectively. This comparison quantifies the difference between the mesh families; the O-grid GCI estimates cannot be assigned to the verification meshes or to their sensitivity maps.

Table 5 and Figure 5 summarize the integrated responses. The Carreau creeping-flow problem also provides an analytical scaling check. Multiplying both limiting viscosities by the same constant preserves the velocity solution and scales the pressure and drag by that constant. Therefore

$$\eta_0 S_{\eta_0} + \eta_\infty S_{\eta_\infty} = \mathcal{D}_0. \tag{24}$$

The normalized sum in Table 5 is 0.998561, a 0.144% departure from this identity. This check tests the combined viscosity response independently of the λ perturbations.

Table 5. Integrated sensitivities on the 17,600-cell verification meshes. $s_i = (\theta_{i,0}/\mathcal{D}_0)S_i$ is dimensionless. The units of S_i^{AD} are N/(Pa s) for viscosities, N/s for λ and N for n. The independent perturbation test is for λ; the remaining parameter entries are adjoint predictions.

Model	Parameter	S_i^{AD}	s_i
Carreau	η_0	3.5972665	0.878305
Carreau	η_∞	492.53321	0.120256
Carreau	λ	−0.02874258	−0.701776
Carreau	n	20.762654	1.013877
Oldroyd-B	η_s	0.10628931	0.651115
Oldroyd-B	η_p	0.080678371	0.343445
Oldroyd-B	λ	−4.6286105	−0.024029

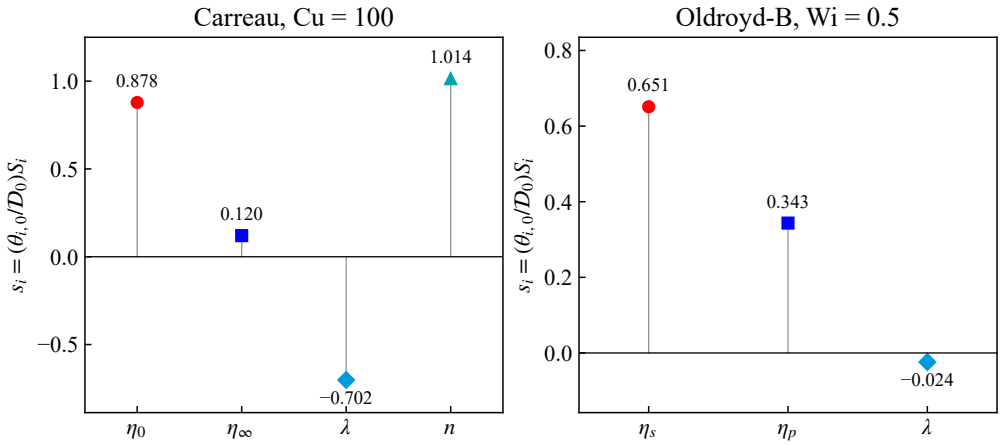


Figure 5. Normalized integrated cylinder sensitivities at the two tested states. The parameters and boundary conditions differ between the models. The λ entries are independently checked by direct perturbations; the other entries are adjoint predictions, with an additional combined-viscosity scaling check for Carreau.

4.2. Carreau Cylinder Fields

The Carreau direct fields in Figure 6 show accelerated flow around the cylinder sides and a nearly antisymmetric transverse velocity. The pressure difference across the body contributes to the same surface-force objective as the viscous traction. A large local strain alone does not determine a drag sensitivity: its influence is weighted by the adjoint response of the complete force objective.

Figure 7 shows the normalized sensitivities. The limiting-viscosity and index responses are predominantly positive; the transition-time response is negative. For $n < 1$, increasing λ reduces the apparent viscosity at a fixed nonzero strain rate, while increasing n weakens shear thinning. The signed integrals reflect these different roles: $s_\lambda = -0.701776$ and $s_n = 1.013877$ at this state. These are first-order responses at the specified parameters, not universal values across the Carreau regime.

The sensitivity to η_∞ emphasizes the high-shear side layers, whereas η_0 retains a larger total normalized contribution. Their global coefficients are 0.120256 and 0.878305. Consequently, an intense local high-shear feature need not dominate the integral. The magnitude, spatial extent and adjoint weighting must all be considered.

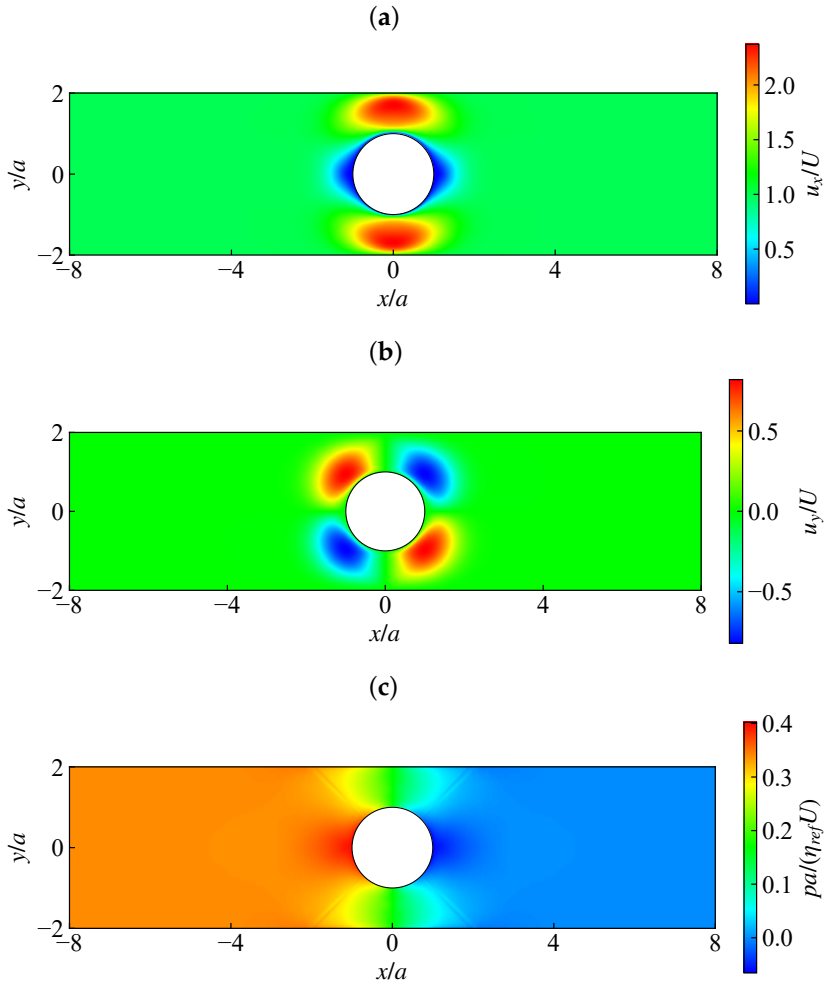


Figure 6. Carreau cylinder direct fields at Cu = 100: (**a**) streamwise velocity, (**b**) transverse velocity and (**c**) normalized pressure.

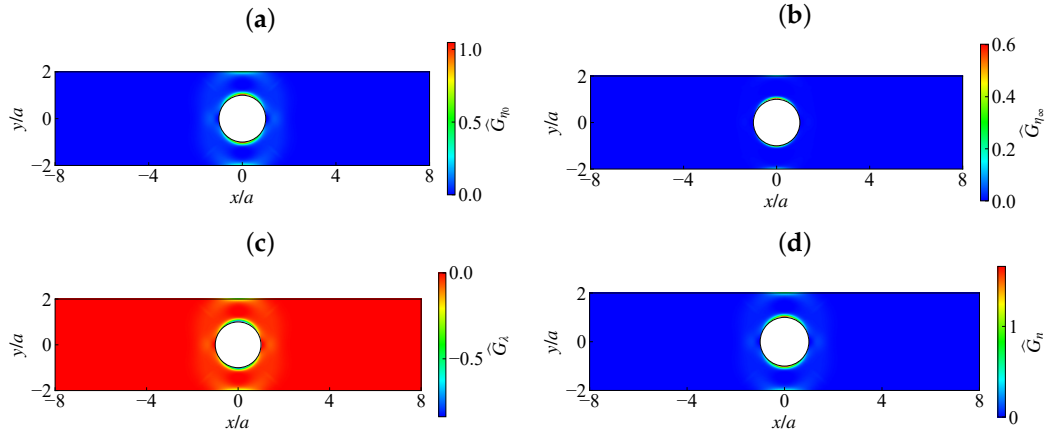


Figure 7. Carreau dimensionless field sensitivities at Cu = 100: (**a**) η_0, (**b**) η_∞, (**c**) λ and (**d**) n. Normalization follows Equation (18). The independent integral check is given in Table 3.

4.3. Oldroyd-B Cylinder Fields and Cancellation

Figure 8 shows the direct fields for standard Oldroyd-B flow. The archived case labeled Oldroyd-B used FENE-P with $L^2 = 10^9$ and gave a total force of 0.0956446845514 N, compared with 0.096312707213 N here. Model representation and discretization both differ, so this change cannot be assigned solely to finite extensibility. The adjoint and perturbed direct solutions used in the derivative check share the same standard Oldroyd-B model and mesh.

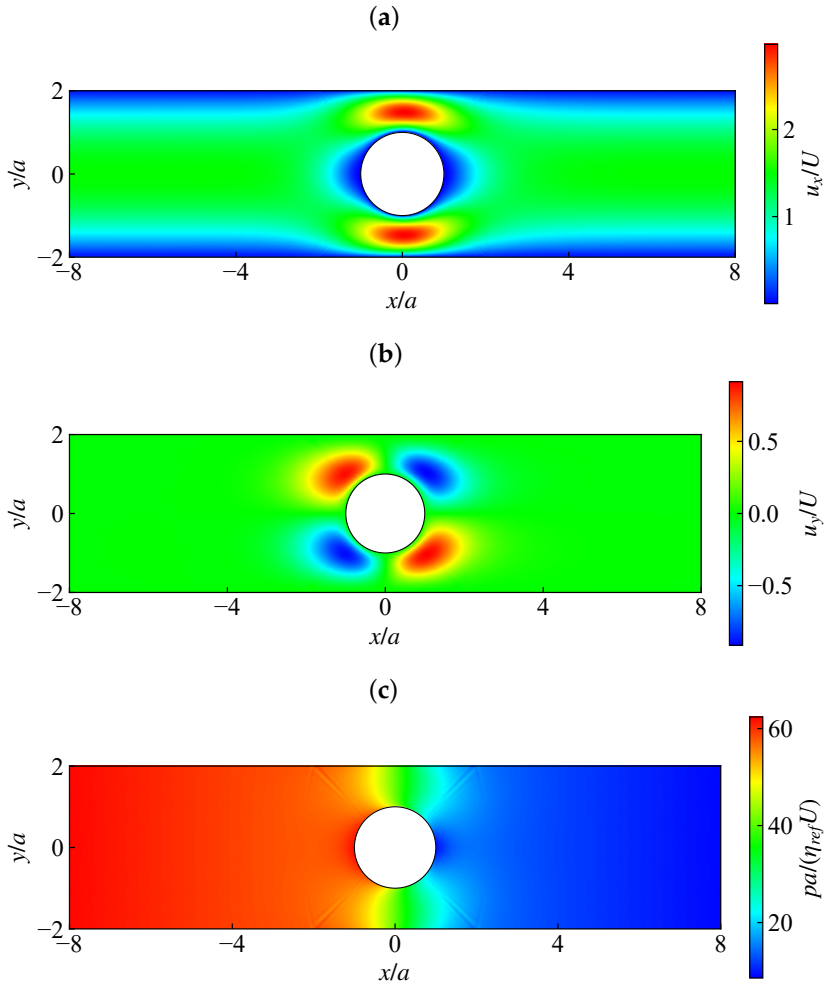


Figure 8. Oldroyd-B cylinder direct fields at Wi = 0.5: (**a**) streamwise velocity, (**b**) transverse velocity and (**c**) normalized pressure. The inlet is parabolic, and the channel walls are stationary.

The solvent and polymer viscosity fields in Figure 9 have dominant positive contributions, but the relaxation-time field contains both signs. Its thin positive near-body layer coexists with negative regions farther from the wall. Integrating the positive and negative parts separately gives $S_\lambda^+ = 18.8504$ and $S_\lambda^- = -23.479$, whose sum is -4.6286105. The net magnitude is only 10.93% of the sum of their absolute magnitudes. This cancellation explains why judging the global response from the largest contour value would be misleading.

This signed structure reflects the upper-convected transport kernel in Equation (16). The finite-difference comparison checks its net volume integral. The separate positive and negative contributions describe the computed field; neither subregion has an independent local verification.

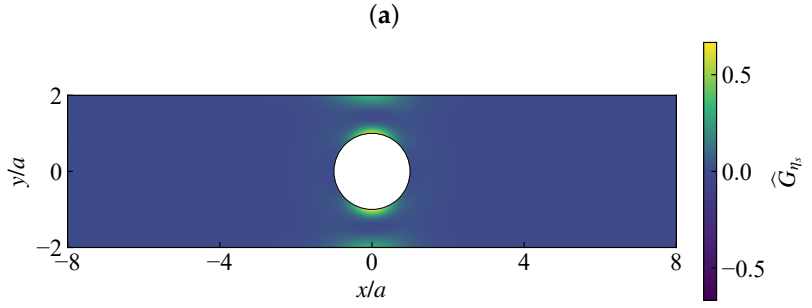


Figure 9. *Cont.*

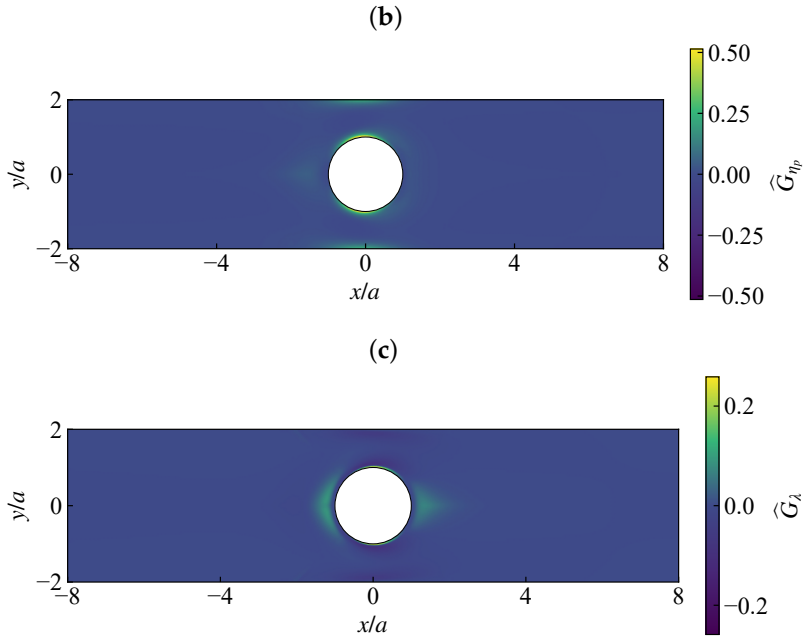


Figure 9. Oldroyd-B dimensionless sensitivities: (**a**) solvent viscosity, (**b**) polymer viscosity and (**c**) relaxation time. The color limits are symmetric about zero; normalization follows Equation (18).

4.4. Archived Confined-Sphere Direct-Flow Illustration

The archived sphere case illustrates the direct-flow response at Cu $= 1$. Figure 10 shows cell/plane intersections at $z = 0$ in the quadrant $x \geq 0$, $y \geq 0$, with $r = y$ and $u_r = u_y$. The high-strain side region has a lower apparent viscosity. The shear rate is reconstructed from the saved viscosity by inverting Equation (4); it is not an independently saved measurement of the velocity gradient.

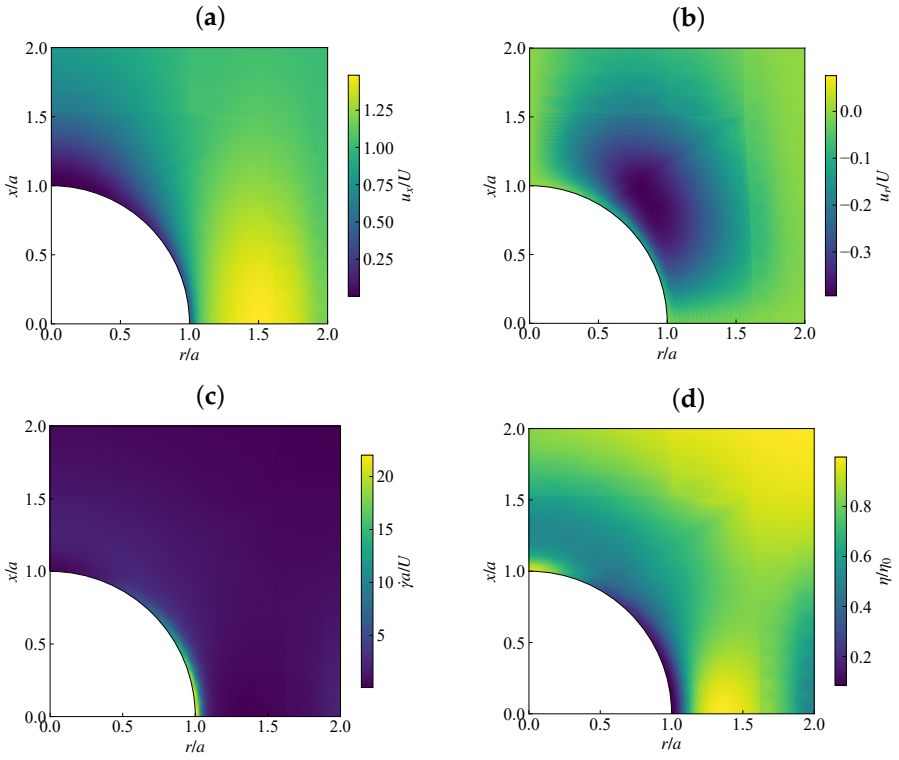


Figure 10. Archived confined-sphere direct fields at Cu $= 1$ in the meridional quadrant $0 \leq r/a, x/a \leq 2$: (**a**) u_x/U, (**b**) u_r/U, (**c**) $\dot{\gamma}a/U$ reconstructed from the Carreau viscosity and (**d**) η/η_0. The axial direction is vertical, as in the original plot, and the coordinate origin is at the sphere center.

Figure 11 combines 23 archived force records with the transition times in their case dictionaries. Drag decreases from the zero-shear-viscosity regime toward the high-shear plateau as $\mathrm{Cu} = \lambda U/a$ increases. The reference $\mathcal{D}_N = 0.00223892$ N is the stored Newtonian force for the same geometry. These results concern direct flow only. The sphere is not included in the verified global-sensitivity results, which are restricted to the cylinder states in Tables 3–5.

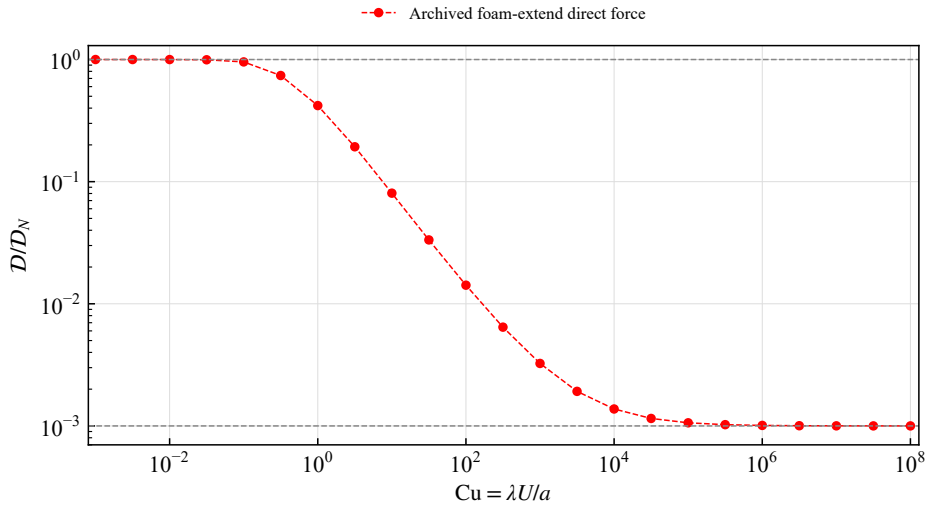


Figure 11. Archived sphere force reconstructed from 23 direct force records and the time scales in their constitutive dictionaries. $\mathcal{D}_N$ is the archived Newtonian reference for the same geometry. The dashed levels mark 1 and $\eta_\infty/\eta_0 = 0.001$. The curve is an archived direct-force result.

4.5. Relation to Archived Direct Benchmarks

Table 6 compares the archived rheoTool resistance values with the MIX0 finite-element reference of Fan et al. [22]. Resistance is normalized by $\eta_{\mathrm{ref}} U L_z$. The relative differences, recalculated from the displayed values, remain below 0.7%. This historical direct-flow comparison is separate from the standard Oldroyd-B derivative checks above.

Table 6. Archived rheoTool large-extensibility cylinder resistance and the MIX0 reference. The last column is $100|D_{\mathrm{arch}} - D_{\mathrm{ref}}|/D_{\mathrm{ref}}$, calculated from the displayed normalized values.

Wi	Archived Result	MIX0 [22]	Relative Difference (%)
0.0	132.44	132.36	0.06
0.1	130.21	130.36	0.12
0.2	126.50	126.62	0.09
0.3	123.13	123.19	0.05
0.4	120.67	120.59	0.07
0.5	118.96	118.83	0.11
0.6	118.01	117.78	0.20
0.7	117.66	117.32	0.29
0.8	117.79	117.36	0.37
0.9	118.24	117.80	0.37
1.0	119.29	118.49	0.68

5. Discussion

The normalized coefficients in Table 5 give a direct interpretation of small uniform parameter changes. A 1% increase in the Carreau transition time predicts approximately a 0.702% decrease in drag; a 1% increase in the shear index predicts approximately a 1.014% increase. These estimates follow from $\delta\mathcal{D}/\mathcal{D}_0 \simeq s_i \delta\theta_i/\theta_{i,0}$, with the other parameters

and boundary data fixed. They concern the local slope at $\mathrm{Cu} = 100$, rather than a trend established over the full parameter range.

The Carreau maps combine the constitutive derivative with the direct–adjoint strain product. The normalized integrals show that the localized high-shear-viscosity response is smaller than the zero-shear-viscosity contribution, despite its pronounced near-body feature. Peak contour values therefore provide an incomplete ranking of parameter influence. This use of local and integrated responses follows the rheological field-sensitivity approach of Freund et al. [14], who considered resistance in a confined-sphere geometry. The present cylinder values are not a quantitative replication of that geometry.

For Oldroyd-B flow, a 1% increase in λ predicts a much smaller drag change, approximately -0.0240%. The small net response does not imply that the local relaxation-time sensitivity is weak: its positive and negative integrals are 18.8504 and $-23.479\ \mathrm{N\,s^{-1}}$, respectively. The net is only 10.93% of their absolute sum. The constitutive transport term in Equation (16) accounts for this signed response. Kim's low-Deborah-number cylinder adjoint [15] provides the relevant viscoelastic formulation, but matching the geometry, inlet profile, viscosity ratio and nondimensionalization would be required for a quantitative comparison. In the present two cases, wall motion and inlet conditions also differ, so their contrast cannot be attributed to constitutive behavior alone.

Figure 12 summarizes the link between a local parameter change and the global drag response.

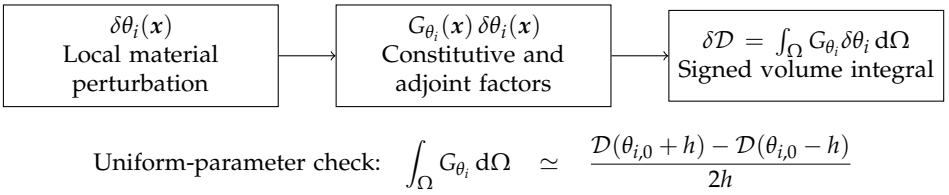


Figure 12. From a local parameter perturbation to the first-order drag response. The middle term combines the constitutive response with the adjoint weighting. Its signed volume integral can be checked by a uniform perturbation of the direct problem. This diagram describes the calculation and is not an additional flow result.

The numerical checks support different parts of this interpretation. The three-grid sequence measures the resolution dependence of direct drag, whereas the finite differences check the integrated λ sensitivity on the separate 17,600-cell meshes. Reducing the perturbation step changes the finite-difference estimate only slightly, leaving a residual discrepancy that can include discretization, boundary truncation and iterative error. A separately discretized continuous adjoint need not return the exact derivative of the discrete direct equations [16]. Agreement at the reported level supports the integral for these states; it does not establish pointwise sensitivity accuracy, cross-grid convergence of the derivative or independent verification of every material parameter.

The Oldroyd-B calculations use upwind stress transport to obtain a converged state at $\mathrm{Wi} = 0.5$. Its numerical diffusion is part of the reported spatial error. Higher elasticity may require formulations such as log-conformation or other stabilization approaches [9,10,20,23]. The archived sphere fields and forces provide direct-flow context, but a three-dimensional adjoint would require its own mesh and perturbation checks. The present results are steady numerical tests; they do not constitute new experimental validation.

6. Conclusions

Finite-volume adjoint sensitivities were computed for two confined cylinder flows and checked against direct parameter perturbations. For the Carreau transition time and the Oldroyd-B relaxation time, the maximum discrepancies over the tested central-difference steps were

0.221% and 0.418%, respectively. Separate refinement sequences gave medium-to-fine drag changes of 0.495% and 0.488%. These results support the reported integrated derivatives at the specified states while keeping force convergence distinct from sensitivity convergence.

For Carreau flow, the normalized transition-time and shear-index derivatives were −0.701776 and 1.013877. Their opposite signs follow the corresponding changes in apparent viscosity. For Oldroyd-B flow, the relaxation-time derivative was negative, although substantial positive contributions occurred near the body; the net integral was only 10.93% of the absolute signed contributions. The local maps are therefore most informative when read together with the volume integrals. Verification of other parameters, local sensitivity convergence and three-dimensional adjoints remains necessary before extending these conclusions beyond the tested cylinder cases.

Supplementary Materials: The following supporting information can be downloaded at: https://www.mdpi.com/article/10.3390/fluids11100255/s1; S1: This numerical reproducibility archive contains solver sources, case files, mesh-generation scripts, convergence histories and verification data.

Author Contributions: Conceptualization, X.L., Z.L. and S.P.; methodology, X.L. and Z.L.; software, X.L. and Z.L.; validation, X.L. and X.W.; formal analysis, X.L. and X.W.; investigation, X.L. and X.W.; resources, X.L.; data curation, X.L.; writing—original draft preparation, X.L. and Z.L.; writing—review and editing, X.W. and S.P.; visualization, X.L.; supervision, S.P.; project administration, X.L.; funding acquisition, S.P. All authors have read and agreed to the published version of the manuscript.

Funding: This research was funded by the National Natural Science Foundation of China, grant number 12501602; the Education Department of Hunan Province, grant number 24C0055; the Science and Technology Department of Hunan Province, grant number 2025JJ60052; and the Scientific Research Start-up Fund of Xiangtan University, grant number KZ0810769.

Institutional Review Board Statement: Not applicable.

Informed Consent Statement: Not applicable.

Data Availability Statement: Solver sources, case dictionaries, mesh-generation scripts, convergence histories and tabulated verification data for the reported cylinder calculations are included in Supplementary Material S1. The original archived benchmark data are available from the corresponding author upon reasonable request.

Acknowledgments: The authors acknowledge the computational and administrative support provided by Xiangtan University.

Conflicts of Interest: The authors declare no conflicts of interest.

Abbreviations

The following abbreviations are used in this manuscript.

CFD	Computational fluid dynamics
GCI	Grid convergence index
OpenFOAM	Open Field Operation and Manipulation
MIX0	Mixed finite-element reference formulation
Wi	Weissenberg number

References

1. Carreau, P.J. Rheological equations from molecular network theories. *Trans. Soc. Rheol.* **1972**, *16*, 99–127. [CrossRef]
2. Oldroyd, J.G. On the formulation of rheological equations of state. *Proc. R. Soc. Lond. A* **1950**, *200*, 523–541. [CrossRef]
3. Bird, R.B.; Armstrong, R.C.; Hassager, O. *Dynamics of Polymeric Liquids, Volume 1: Fluid Mechanics*, 2nd ed.; Wiley-Interscience: New York, NY, USA, 1987.

4. Coelho, P.M.; Pinho, F.T. Vortex shedding in cylinder flow of shear-thinning fluids: I. Identification and demarcation of flow regimes. *J. Non-Newton. Fluid Mech.* **2003**, *110*, 143–176. [CrossRef]
5. Bharti, R.P.; Chhabra, R.P.; Eswaran, V. Steady flow of power law fluids across a circular cylinder. *Can. J. Chem. Eng.* **2006**, *84*, 406–421. [CrossRef]
6. Lashgari, I.; Pralits, J.O.; Giannetti, F.; Brandt, L. First instability of the flow of shear-thinning and shear-thickening fluids past a circular cylinder. *J. Fluid Mech.* **2012**, *701*, 201–227. [CrossRef]
7. Bailoor, S.; Seo, J.H.; Mittal, R. Vortex shedding from a circular cylinder in shear-thinning Carreau fluids. *Phys. Fluids* **2019**, *31*, 011703. [CrossRef]
8. Chilcott, M.D.; Rallison, J.M. Creeping flow of dilute polymer solutions past cylinders and spheres. *J. Non-Newton. Fluid Mech.* **1988**, *29*, 381–432. [CrossRef]
9. Hulsen, M.A.; Fattal, R.; Kupferman, R. Flow of viscoelastic fluids past a cylinder at high Weissenberg number: Stabilized simulations using matrix logarithms. *J. Non-Newton. Fluid Mech.* **2005**, *127*, 27–39. [CrossRef]
10. Alves, M.A.; Oliveira, P.J.; Pinho, F.T. Numerical methods for viscoelastic fluid flows. *Annu. Rev. Fluid Mech.* **2021**, *53*, 509–541. [CrossRef]
11. Jameson, A. Aerodynamic design via control theory. *J. Sci. Comput.* **1988**, *3*, 233–260. [CrossRef]
12. Giles, M.B.; Pierce, N.A. An introduction to the adjoint approach to design. *Flow Turbul. Combust.* **2000**, *65*, 393–415. [CrossRef]
13. Othmer, C. A continuous adjoint formulation for the computation of topological and surface sensitivities of ducted flows. *Int. J. Numer. Methods Fluids* **2008**, *58*, 861–877. [CrossRef]
14. Freund, J.B.; Kim, J.; Ewoldt, R.H. Field sensitivity of flow predictions to rheological parameters. *J. Non-Newton. Fluid Mech.* **2018**, *257*, 71–82. [CrossRef]
15. Kim, J. Adjoint-based sensitivity analysis of viscoelastic fluids at a low Deborah number. *Appl. Math. Model.* **2023**, *115*, 453–469. [CrossRef]
16. Nadarajah, S.; Jameson, A. A comparison of the continuous and discrete adjoint approach to automatic aerodynamic optimization. In Proceedings of the 38th Aerospace Sciences Meeting and Exhibit, Reno, NV, USA, 10–13 January 2000; AIAA Paper 2000-0667. [CrossRef]
17. Jasak, H. Error Analysis and Estimation for the Finite Volume Method with Applications to Fluid Flows. Ph.D. Thesis, Imperial College London, London, UK, 1996.
18. Weller, H.G.; Tabor, G.; Jasak, H.; Fureby, C. A tensorial approach to computational continuum mechanics using object-oriented techniques. *Comput. Phys.* **1998**, *12*, 620–631. [CrossRef]
19. Favero, J.L.; Secchi, A.R.; Cardozo, N.S.M.; Jasak, H. Viscoelastic flow analysis using the software OpenFOAM and differential constitutive equations. *J. Non-Newton. Fluid Mech.* **2010**, *165*, 1625–1636. [CrossRef]
20. Pimenta, F.; Alves, M.A. Stabilization of an open-source finite-volume solver for viscoelastic fluid flows. *J. Non-Newton. Fluid Mech.* **2017**, *239*, 85–104. [CrossRef]
21. Celik, I.B.; Ghia, U.; Roache, P.J.; Freitas, C.J.; Coleman, H.; Raad, P.E. Procedure for estimation and reporting of uncertainty due to discretization in CFD applications. *J. Fluids Eng.* **2008**, *130*, 078001. [CrossRef]
22. Fan, Y.; Tanner, R.I.; Phan-Thien, N. Galerkin/least-square finite-element methods for steady viscoelastic flows. *J. Non-Newton. Fluid Mech.* **1999**, *84*, 233–256. [CrossRef]
23. Fattal, R.; Kupferman, R. Constitutive laws for the matrix-logarithm of the conformation tensor. *J. Non-Newton. Fluid Mech.* **2004**, *123*, 281–285. [CrossRef]

Disclaimer/Publisher's Note: The statements, opinions and data contained in all publications are solely those of the individual author(s) and contributor(s) and not of MDPI and/or the editor(s). MDPI and/or the editor(s) disclaim responsibility for any injury to people or property resulting from any ideas, methods, instructions or products referred to in the content.